Supporting Information

Interaction-induced Self-assembly of Au@La$_2$O$_3$ Core-shell Nanoparticles on La$_2$O$_2$CO$_3$ Nanorods with Enhanced Catalytic Activity and Stability for Soot Oxidation
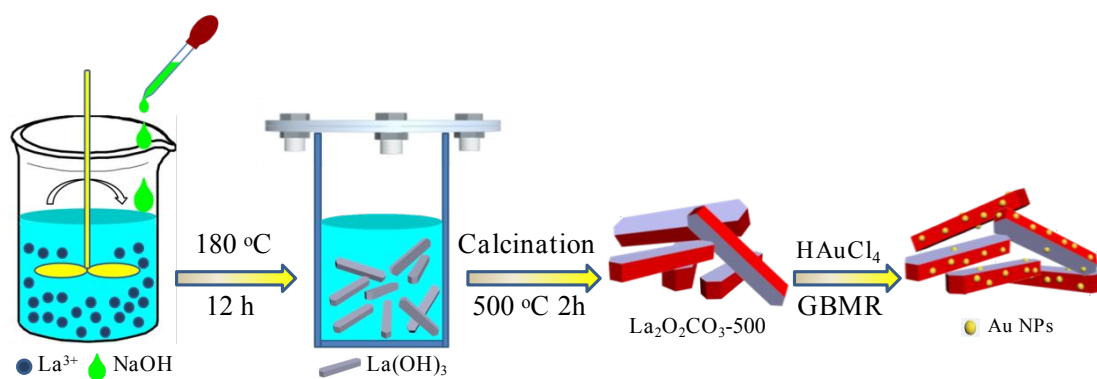
Qiangqiang Wu, Jing Xiong, Yilin Zhang, Xuelei Mei, Yuechang Wei*, Zhen Zhao,

Jian Liu, and Jianmei Li

State Key Laboratory of Heavy Oil Processing, College of Science, China University

of Petroleum, Beijing 102249, China

* Corresponding author. Email address: weiyc@cup.edu.cn

Postal Address: 18# Fuxue Road, Chang Ping District, Beijing, 102249, China,
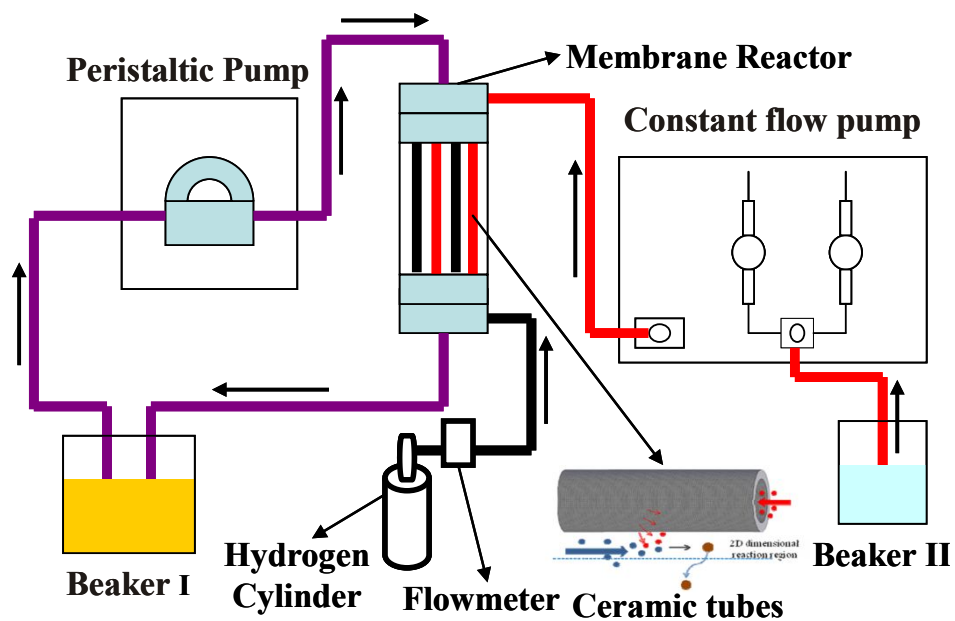
Tel: 86-10-89731586, Fax: 86-10-69724721

Figure S1 Schematic Process for the preparation of $Au_n/La_2O_2CO_3$-500 catalysts.

1. Synthetic process of $La_2O_2CO_3$-500 nanorods supported Au nanoparticle catalysts.
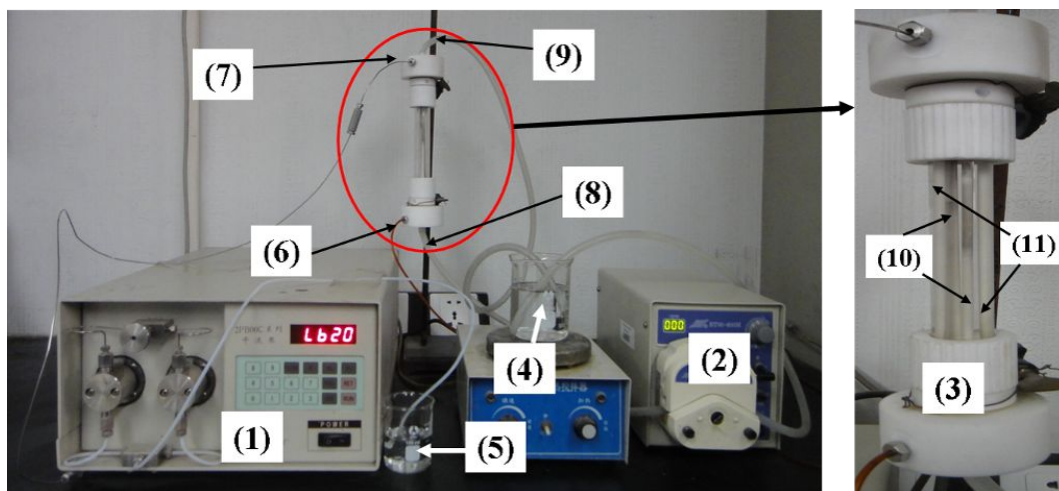
The effective controlling of the dispersion and size of supported Au particles on the surface of $La_2O_2CO_3$-500 nanorods is a primary goal of catalyst design and is quite challenging. Generally, the nucleation and growth of metal nanocrystals govern the particle size and morphology of the nanoparticles in the synthesis process of supported Au nanoparticles (NPs) by coprecipitation or reduction.[1,2] The loading of Au NPs on the surface of $La_2O_2CO_3$-500 nanorods is carried out by a GBMR method, whose detailed information is shown in Figure S2-S4. The ceramic membrane reactor is the core equipment of GBMR method and is composed of four ceramic membrane tubes, two tubes are used for highly homogeneous dispersion of $NaBH_4$ solution (as a reductant) and the other two used for dispersion of H_2 gas bubbling instead of mechanical stirring. The dispersion rate of $NaBH_4$ solution and the size of gas bubbling are controlled by the size of holes (d = 40 nm) on ceramic membrane tubes. The reductive H_2 gas bubbling not only promote mass transfer, and reduce concentration gradient of reductant to improve the homogeneity of $NaBH_4$ solution, but also provide a reducing atmosphere which is useful for the reduction of Au ions. The highly homogeneous dispersion of reductant is an operative means to regulate the nucleation process of Au NPs so as producing a mass of Au nucleus. The numerous small crystallites (Au nucleus) on the surface of $La_2O_2CO_3$-500 nanorods tend to quickly aggregate together to form larger and more thermodynamically stable particles (growth).[3] However, the addition of organic stability reagent into precursor solution can regulate the growth process. Consequently, the highly dispersed and uniformed Au NPs are supported on the surface of $La_2O_2CO_3$-500 nanorods.

In the synthesis process of samples, $AuCl_4^-$ ions are adsorbed and anchored on

surface La^{3+}-O^{2-} pairs of the $La_2O_2CO_3$-500 nanorods. Meanwhile, the hybrid between $AuCl_4^-$ ions and capping ligands of the poly N-vinyl-2-pyrrolidone (PVP) might form. The reduction of $AuCl_4^-$ occurred immediately to give Au nucleus (nucleation) when $NaBH_4$ solution was introduced into the membrane reactor, resulting in restriction of the growth of crystal nucleus on the surface of $La_2O_2CO_3$-500 nanorods due to the protection of PVP. Therefore, the supported Au particle size can be effectively controlled by the PVP concentration, and the uniform distribution of Au particles can be further improved by highly homogeneous dispersion of $NaBH_4$ solution, which depends on the hole size of the ceramic membrane tubes, the flow rate of $NaBH_4$ solution and the stirring of the hydrogen gas bubbling.

Figure S2 Schematic representation of gas bubbling-assisted membrane reduction (GBMR) device for the synthesis of $Au_n/La_2O_2CO_3$-500 catalysts.

Figure S3 The digital photos of GBMR device. The right section in the photos is the ceramic membrane reactor composed of four ceramic membrane tubes, which is the core of the device of GBMR method.

(1) The constant flow pump (HLB-2020, Satellite Manufactory of Beijing, P.R. China).

(2) The peristaltic pump (BT00-600M, Baoding Lange Co., Ltd, P.R. China).

(3) The ceramic membrane reactor consisted of four ceramic membrane tubes (Φ 3 mm $\times$ 160 mm, Hyflux Group of Companies, Singapore), which is the core of the device of GBMR method.

(4) Beaker I filled with mixture solution ($HAuCl_4$ solution, PVP and $La_2O_2CO_3$-500 nanorods).

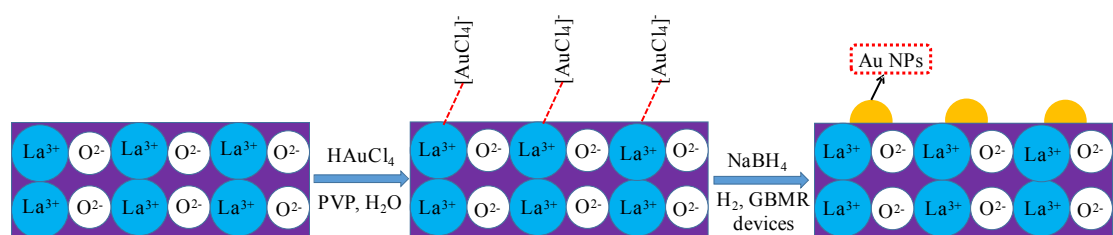(5) Beaker II filled with $NaBH_4$ solution (reductant).

(6) The inlet of hydrogen.

(7) The inlet of $NaBH_4$ solution (reductant).

(8) The inlet of mixture solution.

(9) The outlet of mixture solution and hydrogen.

(10) Two ceramic membrane tubes used for the dispersion of $NaBH_4$ solution (reductant).

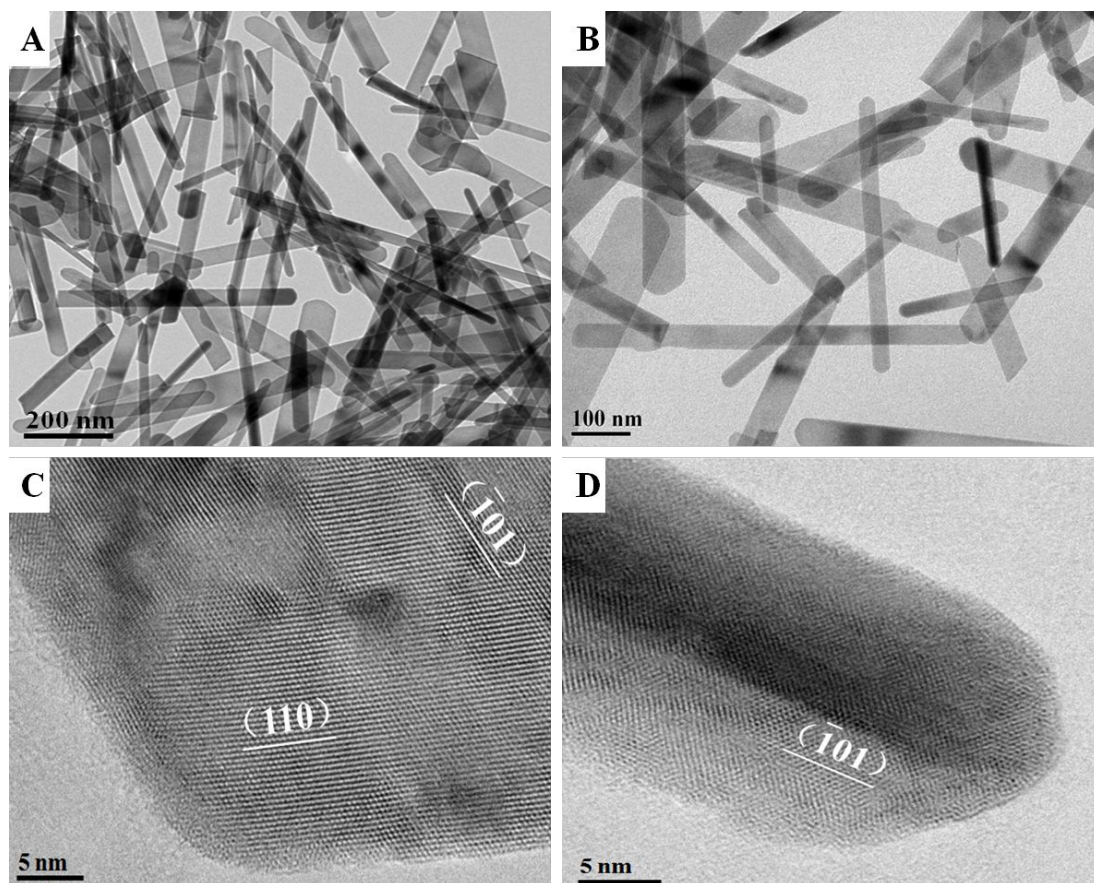(11) Two ceramic membrane tubes used for the dispersion of hydrogen bubbling.

Figure S4 Schematic representation for the synthesis of gold nanoparticles (NPs) on the surface of $La_2O_2CO_3$-500 nanorods by the GBMR method.
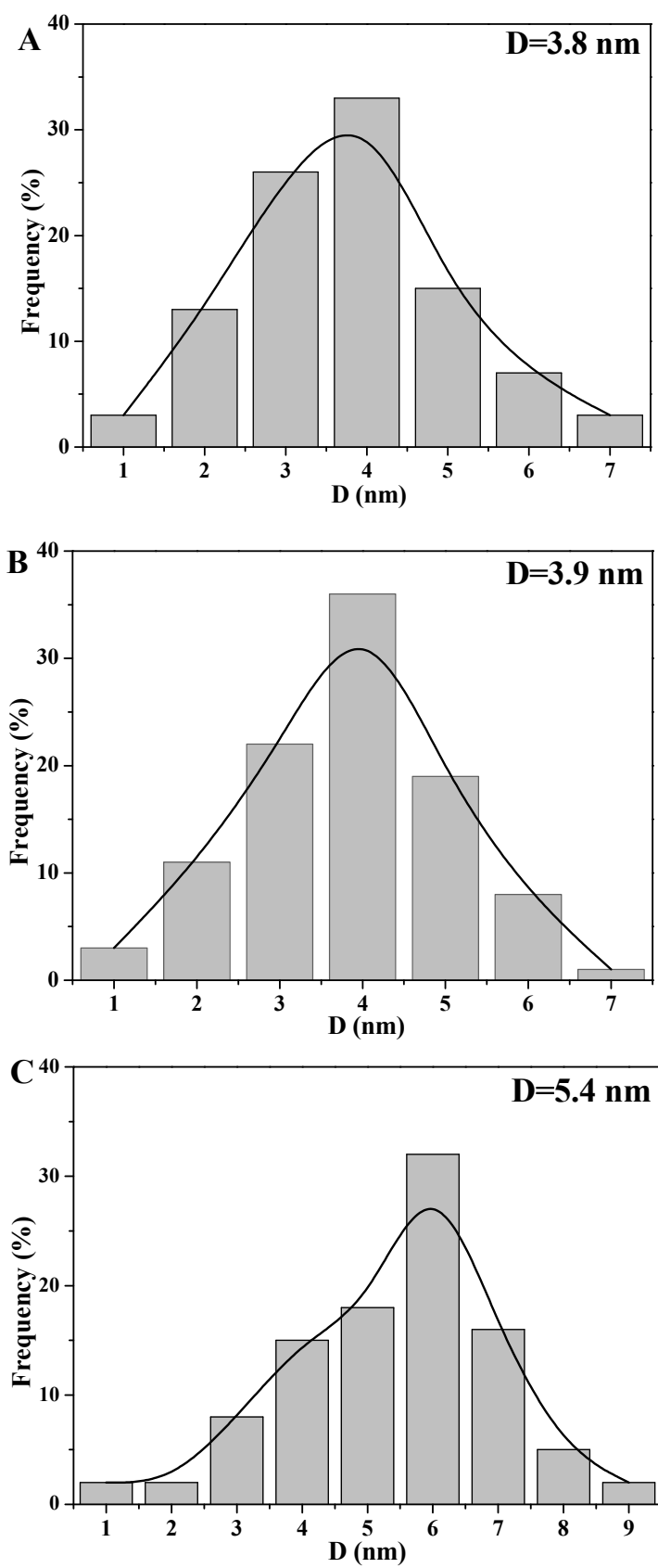
2. The phase change of La(OH)$_3$ nanorods under calcination.

As shown in Figure S5, the La(OH)$_3$ nanorods exhibited characteristic diffraction lines of pure hexagonal phase (JCPDS 36-1481). However, calcination of this hydroxide precursor at 500 ^{o}C for 2 h in air yielded different characteristic peaks from La(OH)$_3$, which corresponded to a pure hexagonal La$_2$O$_2$CO$_3$ phase (JCPDS 37-0804). Further raising the temperature to 600 ^{o}C, the reflections of hexagonal La$_2$O$_2$CO$_3$ weakened whereas La$_2$O$_3$ (JCPDS 05-0602) emerged, indicating the transformation of La$_2$O$_2$CO$_3$ to La$_2$O$_3$. At 700 ^{o}C, the diffraction lines of La$_2$O$_2$CO$_3$ have entirely vanished and the diffraction lines were readily indexed to pure hexagonal La$_2$O$_3$ phase. Raman spectra also supported the crystalline phase transformation of La(OH)$_3$ nanorods. The Raman spectra for all the samples are shown in Figure 3. The La(OH)$_3$ precursor exhibited four distinct bands at 287, 337, 455, and 599 cm^{-1}. After calcination at 500 ^{o}C for 2 h in air, four bands at 372, 393, 779, and 1087cm^{-1} and a minor band at 1062 cm^{-1} were observed at 100-1200 cm^{-1} region, while are assigned to the hexagonal La$_2$O$_2$CO$_3$ (JCPDS 37-0804). With the increase of the temperature to 700 ^{o}C, four bands at 285, 345, 455 and 1078 cm^{-1} were clearly observed because of the formation of pure hexagonal La$_2$O$_3$.[4,5,6] The crystal phase structures of hexagonal La$_2$O$_2$CO$_3$ and La$_2$O$_3$ coexist in the La$_2$O$_2$CO$_3$-550, La$_2$O$_2$CO$_3$-600 and La$_2$O$_2$CO$_3$-650 nanorods. With the increase of the calcined temperature, the intensity of diffraction peaks corresponding to La$_2$O$_3$ phase increases, indicating that the La$_2$O$_2$CO$_3$ phase gradually transforms into La$_2$O$_3$ phase. Consequently, these XRD and Raman results suggest that the synthesized La(OH)$_3$ nanorods are reasonably assumed to have been completely transformed into La$_2$O$_2$CO$_3$ via calcination in air at 500 °C for 2h and into La$_2$O$_3$ via calcination in air at 700 °C for 2 h.
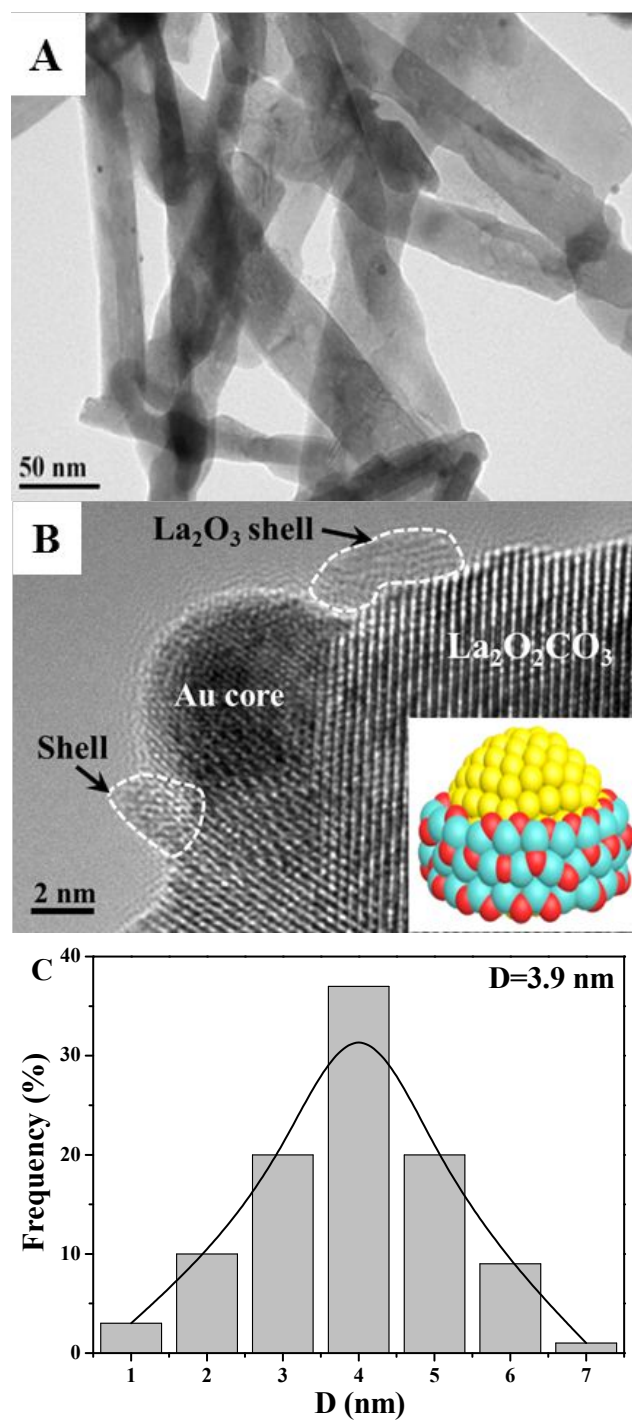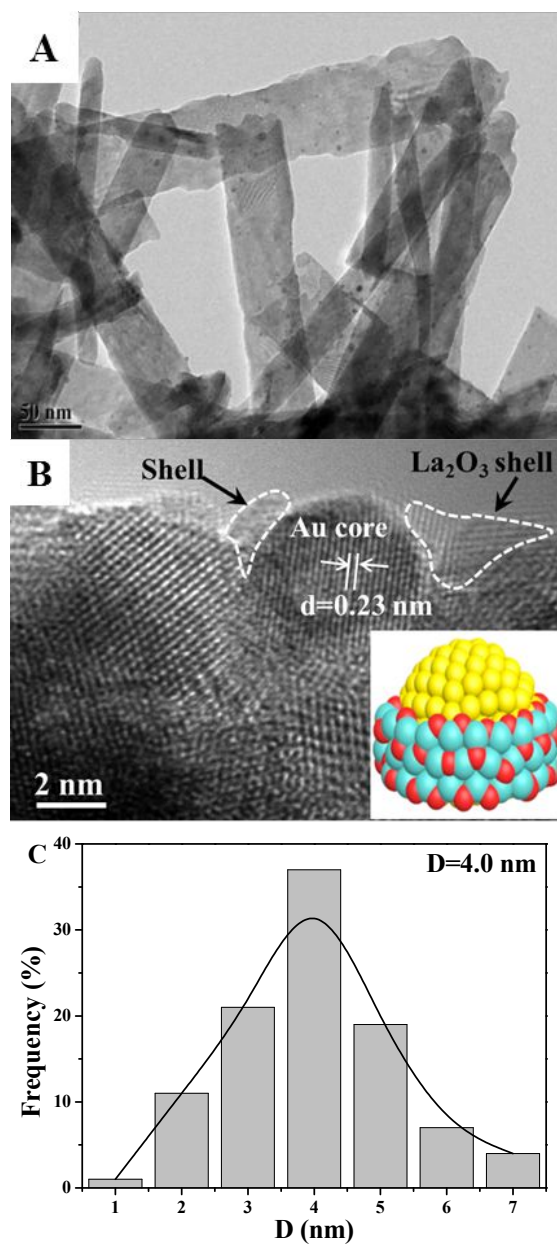
Figure S5 TEM (A-B) and HRTEM (C-D) images of the La(OH)$_3$ nanorods.

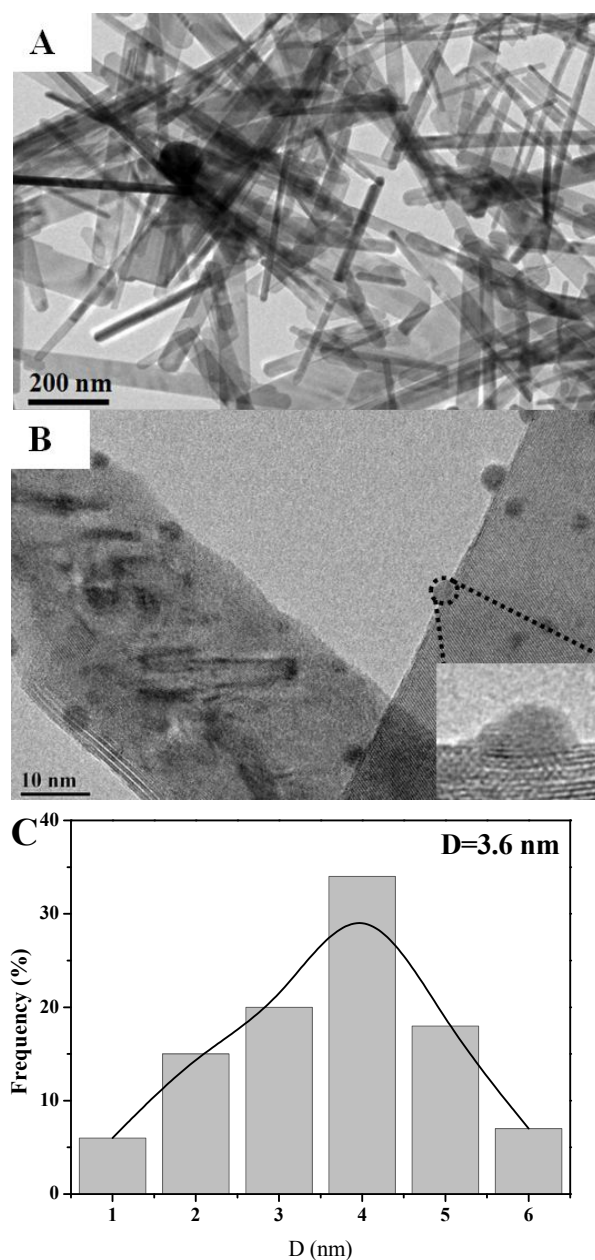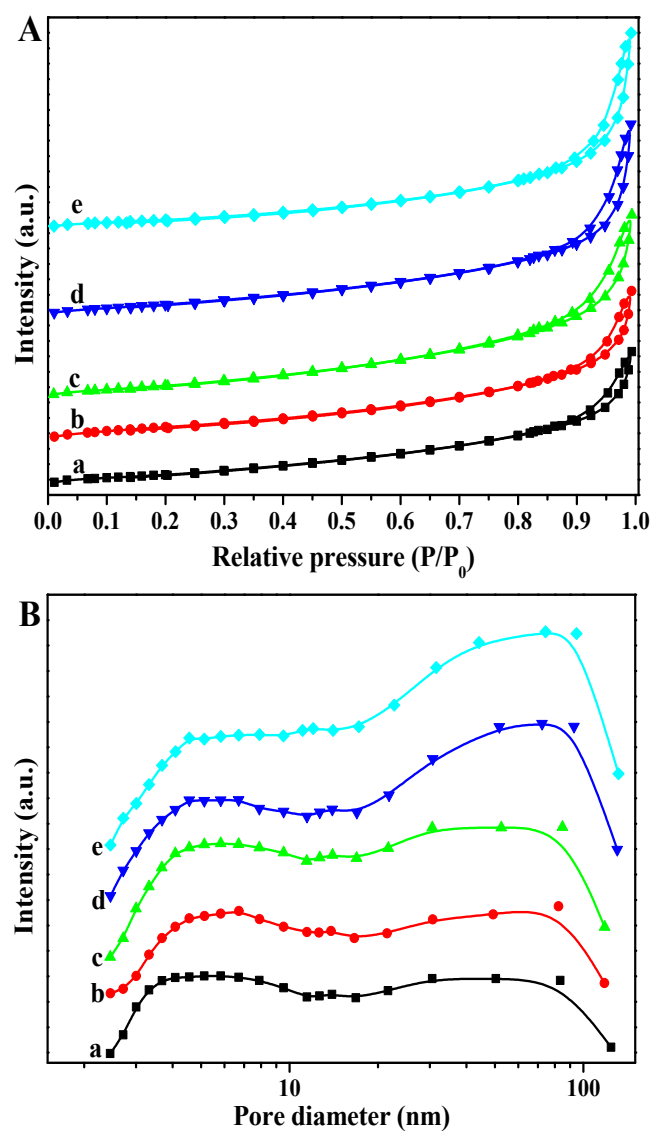**Figure S6** The size distributions of supported Au NPs over $Au_2@La_2O_3$/LOC-R (A), $Au_4@La_2O_3$/LOC-R (B) and Au_4/LOC-R (C) catalysts.

Figure S7 TEM (A), HRTEM (B) images and size distribution (C) of Au NPs in the Au$_1$@La$_2$O$_3$/LOC-R catalyst.

Figure S8 TEM (A), HRTEM (B) images and size distribution (C) of Au NPs in the Au$_6$@La$_2$O$_3$/LOC-R catalyst.

Figure S9 TEM (A) and HRTEM (B) images and size distribution (C) of Au NPs in the $Au_4/La_2O_2CO_3$-500 precursor (without calcination at 600 °C).

Figure S10 The N_2 adsorption-desorption isotherms (A) and pore-size distributions (B) of $La_2O_2CO_3$ and $Au_n@La_2O_3/LOC\text{-}R$ catalysts. a. $La_2O_2CO_3$; b. $Au_1@La_2O_3/LOC\text{-}R$; c. $Au_2@La_2O_3/LOC\text{-}R$; d. $Au_4@La_2O_3/LOC\text{-}R$; e. $Au_6@La_2O_3/LOC\text{-}R$.

Table S1 BET surface areas, pore volumes, median pore diameters and average particle sizes of the $Au_n@La_2O_3/LOC-R$ catalysts.

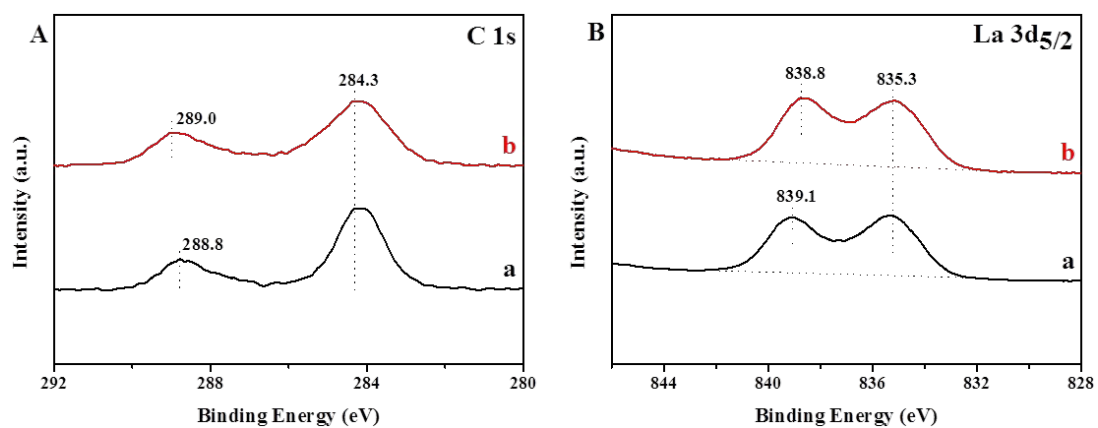| Catalyst	S_{BET}[a] $(m^2\ g^{-1})$	V_p[b] $(cm^3\ g^{-1})$	D_p[c] (nm)	Au size[d] (nm)	Au content[e] $(wt\%)$
$La_2O_2CO_3$-500	42	0.17	10.3	-	-
$La_2O_2CO_3$	40	0.15	9.7	-	-
$Au_1@La_2O_3/LOC-R$	43	0.17	10.6	3.9	0.8
$Au_2@La_2O_3/LOC-R$	44	0.18	10.7	3.8	1.7
$Au_4@La_2O_3/LOC-R$	45	0.19	11.1	3.9	3.7
$Au_6@La_2O_3/LOC-R$	45	0.19	11.3	4.0	5.5
$Au_4/LOC-R$	41	0.16	10.2	5.4	3.6

a Surface area obtained by BET method.

b Pore volume determined by BET method.
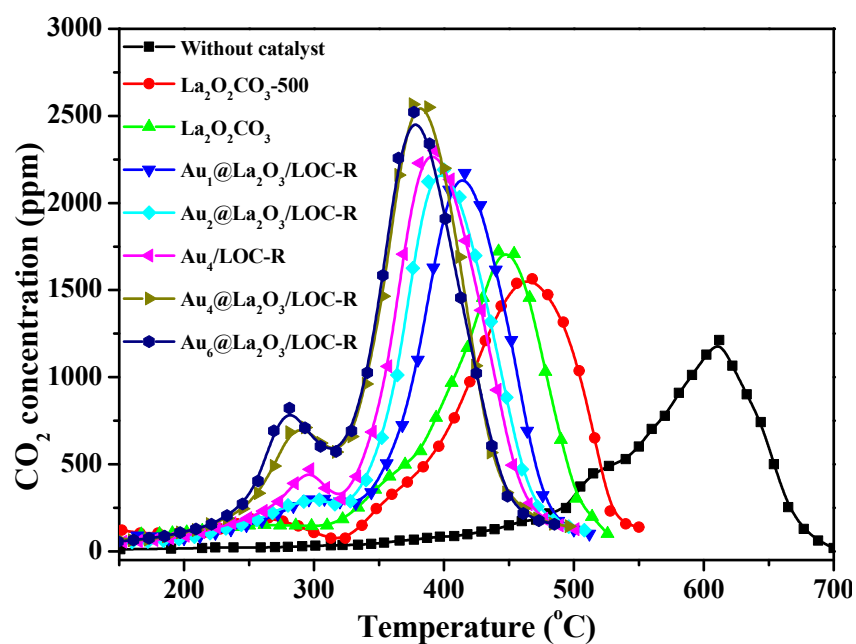
c The median pore diameter determined by BJH method.

d Determined by statistical analysis of more than 100 NPs in many HRTEM images.
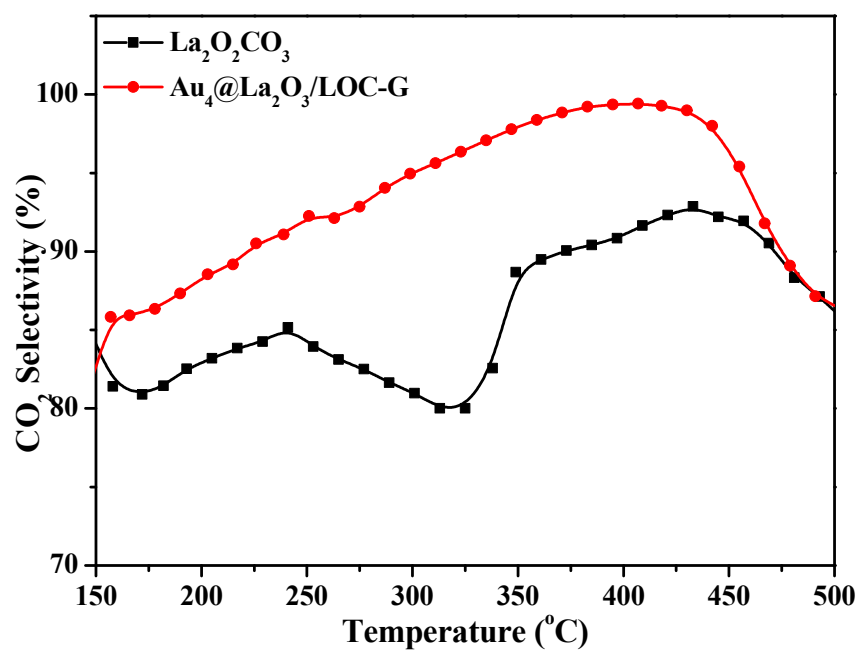
e Determined by ICP-OES.

Figure S11 XPS spectra of C 1s (A) and La $3d_{5/2}$ (B) regions for $La_2O_2CO_3$ (a) and $Au_4@La_2O_3$/LOC-R (b) catalysts.
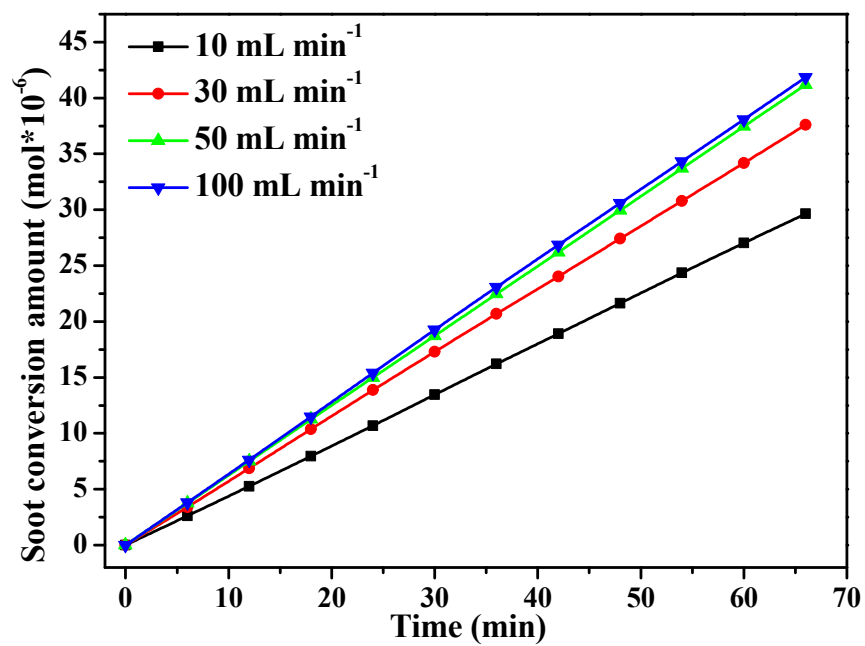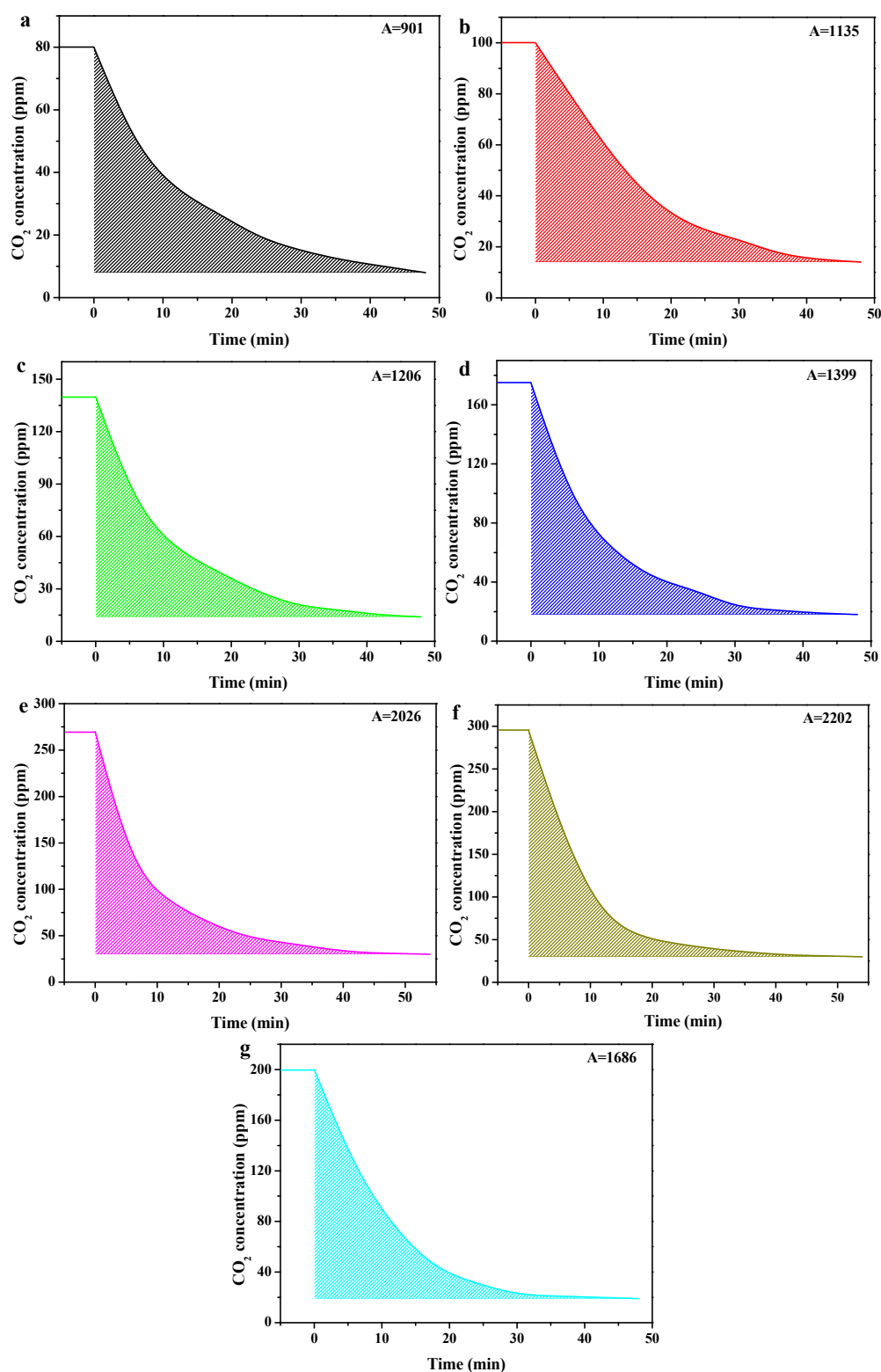
Figure S12 The CO_2 concentration of $La_2O_2CO_3$ nonorods and supported Au nanoparticle catalysts for soot oxidation under conditions of loose contact between soot particles and catalysts.
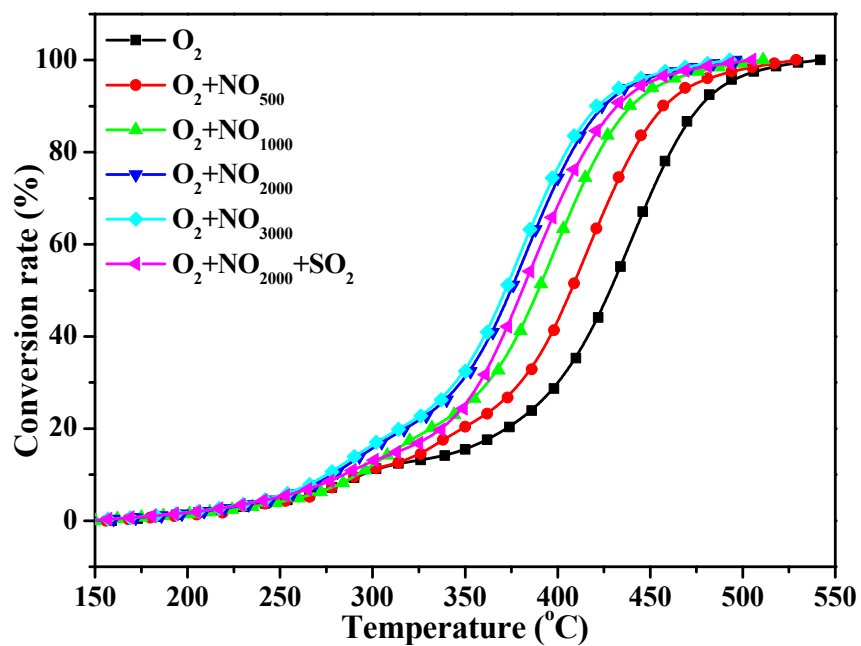
Figure S13 The S_{CO2} profiles of soot oxidation over $La_2O_2CO_3$ and $Au_4@La_2O_3/LOC$-R catalysts.
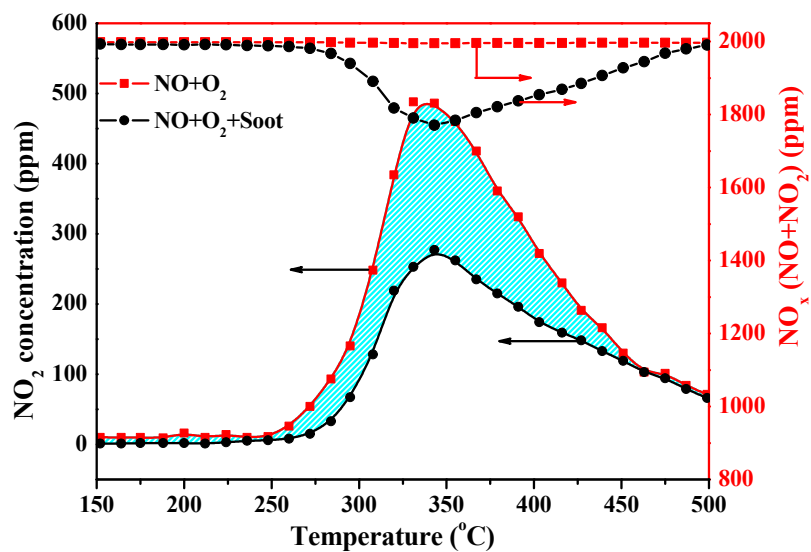
Figure S14 Soot conversion amounts as a function of time over Au$_4$@La$_2$O$_3$/LOC-R catalyst with different the flow rate of reactant gas (10, 30, 50 and 100 ml min^{-1}) at 300 ^{o}C.
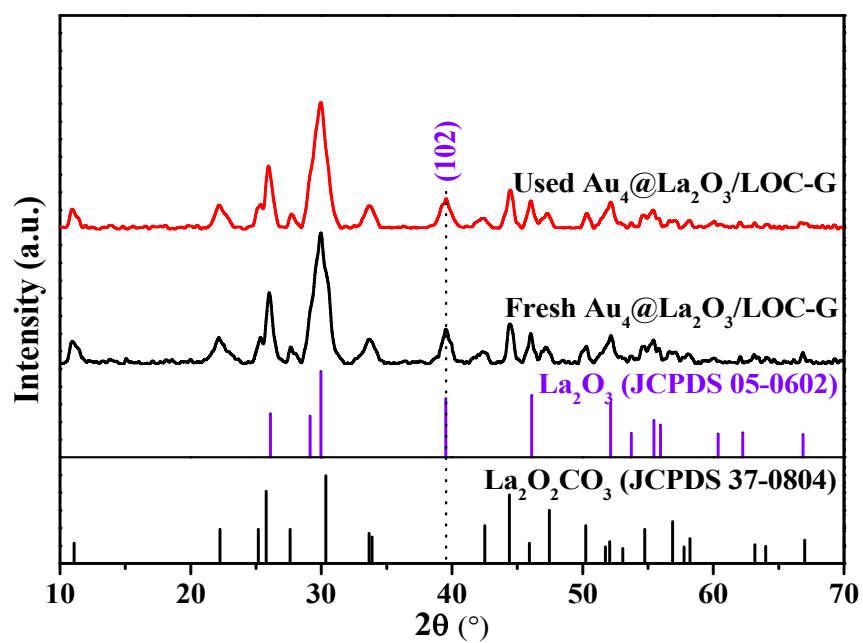
Figure S15 The CO_2 concentrations at 300 °C as a function of time over $Au_n@La_2O_3$/LOC-R catalysts after O_2 is removed from the reactant feed. a. $La_2O_2CO_3$-500; b. $La_2O_2CO_3$; c. $Au_1@La_2O_3$/LOC-R; d. $Au_2@La_2O_3$/LOC-R; e. $Au_4@La_2O_3$/LOC-R; f. $Au_6@La_2O_3$/LOC-R; g. Au_4/LOC-R.
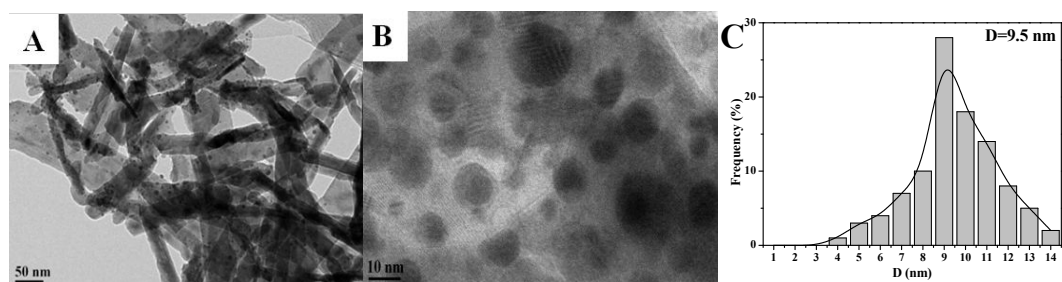
Figure S16 The influence of NO and SO$_2$ on the catalytic activity for soot oxidation over Au$_4$@La$_2$O$_3$/LOC-R catalyst. (O$_2$: 5vol%, NO: 500-3000 ppm, SO$_2$:100 ppm, Ar: balance gas, total gas flow: 50 mL min^{-1}).

Figure S17. The curves of NO_2 and NO_x ($NO+NO_2$) concentration over $Au_4@La_2O_3/LOC-R$ catalyst during NO-TPO and soot-TPO catalytic tests. The blue shadow area corresponds to the consumption of NO_2 for soot oxidation.

Figure S18 XRD patterns of fresh and used (eight soot-TPO cycles) Au$_4$@La$_2$O$_3$/LOC-R catalysts.

Figure S19 TEM (A), HRTEM (B) images and size distribution (C) of supported Au NPs over Au_4/LOC-R catalyst after eight cycles of soot-TPO tests.

References

(1) Zheng, N.; Stucky, G. D. A General Synthetic Strategy for Oxide-Supported Metal Nanoparticle Catalysts. *J. Am. Chem. Soc.* **2006**, *128*, 14278-14280.

(2) Datta, K. K. R.; Reddy, B. V. S.; Ariga, K.; Vinu, A. Gold Nanoparticles Embedded in a Mesoporous Carbon Nitride Stabilizer for Highly Efficient Three-Component Coupling Reaction. *Angew. Chem., Int. Ed.* **2010**, *49*, 5961-5965.

(3) Cushing, B. L.; Kolesnichenko, V. L.; O'Connor, C. J. Recent Advances in the Liquid-Phase Syntheses of Inorganic Nanoparticles. *Chem. Rev.* **2004**, *104*, 3893-3946.

(4) Cornaglia, L. M.; Múnera, J.; Irusta, S.; Lombardo, E. A. Raman Studies of Rh and Pt on La_2O_3 Catalysts Used in a Membrane Reactor for Hydrogen Production. *Appl. Catal. A* **2004**, *263*, 91-101.

(5) Turcotte, R. P.; Sawyer, J. O.; Eyring, L. Rare Earth Dioxymonocarbonates and Their Decomposition. *Inorg. Chem.* **1969**, *8*, 238-246.

(6) Wang, F.; Shi, R.; Liu, Z. Q.; Shang, P. J.; Pang, X.; Shen, S.; Feng, Z.; Li, C.; Shen, W. Highly Efficient Dehydrogenation of Primary Aliphatic Alcohols Catalyzed by Cu Nanoparticles Dispersed on Rod-Shaped $La_2O_2CO_3$. *ACS Catal.* **2013**, *3*, 890-894.